

Collective Excitations of Self-Gravitating Bose-Einstein Condensates: Breathing Mode and Appearance of Anisotropy under Self-Gravity

Kenta Asakawa^{1,*}, Hideki Ishihara^{1,2,†} and Makoto Tsubota^{1,2,‡}

¹ *Department of Physics, Osaka Metropolitan University,
3-3-138 Sugimoto, Sumiyoshi-Ku, Osaka 558-8585,*

Japan ² *Nambu Yoichiro Institute of Theoretical and Experimental Physics (NITEP),
Osaka Metropolitan University, 3-3-138 Sugimoto, Sumiyoshi-Ku, Osaka 558-8585, Japan*

(Dated: July 27, 2023)

We study the collective mode of self-gravitating Bose-Einstein condensates (BECs) described by the Gross-Pitaevskii-Poisson (GPP) equation. The self-gravitating BEC recently receives significant attention in cosmology and astrophysics as a candidate for dark matter. We investigate the breathing and anisotropic collective modes by numerically solving the GPP equation and using the variational method. The breathing mode shows that the period decreases with the total mass due to the density dependence of the self-gravitating BEC, which is quantitatively consistent with our analytical results. We also obtain an anisotropic collective mode, in which the quadrupole mode is coupled with the breathing mode. The period of the quadrupole mode has the same total mass dependence as that of the breathing mode. The characteristics of these periods are different from those of ordinary BECs trapped by an external potential. However, despite the difference in density dependence, their ratio is equal to that of the BEC trapped by an isotropic harmonic potential. Furthermore, a variational method extended to a spheroidal configuration shows that we extract only the quadrupole mode from the anisotropic collective mode.

I. INTRODUCTION

Quantum fluids such as superfluids ^4He , ^3He , and atomic Bose-Einstein condensates (BECs) have been studied in low temperature physics [1, 2]. The emergence of order parameters through spontaneous symmetry breaking is a characteristic of quantum fluids. Because of these characteristics, quantum fluids have been used to understand astrophysical phenomena [3] such as the Kibble-Zurek (KZ) mechanism [4–7] and Hawking radiation by acoustic black holes [8–10]. In this context, we theoretically and numerically investigate self-gravitating BECs, motivated by the conjecture that dark matter (DM) causes Bose-Einstein condensation [11–18].

Various studies of quantum fluids using BECs have been conducted in low temperature physics [1, 2, 19]. The experimental realization of BECs was achieved by laser cooling of atomic Bose gas [2, 20]. Atomic BECs offer several significant advantages over other types of systems. Experimentally, BECs enable us to visualize the condensate density easily and modulate the interatomic interaction using the Feshbach resonance [21]. Theoretically, the Gross-Pitaevskii (GP) equation quantitatively describes a BEC near zero temperature, which represents the time evolution of a macroscopic wave function [1, 2, 22, 23]. Therefore, BECs have been used for various phenomena in quantum simulators [24], quantum information [25], quantum hydrodynamics, and turbulence [26, 27].

Recently, studies of BECs have been extended to astrophysics. BECs are considered candidates for dark matter

halos and are called BEC dark matter (BECDM) [28, 29]. Dark matter (DM) is a hypothetical material that does not emit, reflect, or absorb light. This material can cover galaxies in the form of clumps, which are known as DM halos. In present astrophysics, the DM should play a crucial role as a source of gravity in the Universe because, despite its optical invisibility, the gravity of the DM can affect the rotational motion of galaxies [30] and gravitational lensing [31] [32]. Particularly, the model assuming the existence of non-relativistic dark matter is called the "cold" DM (CDM) model, which succeeds in describing the large-scale structures of the universe [33]. This model is currently regarded as the standard cosmological model. However, this model also has serious discrepancies at small scales between the observational and theoretical results [34].

Several alternatives have been proposed to resolve these problems. The scalar field DM assumes that ultra-light scalar bosons behave as DM [35, 36]. This model can reproduce the results of CDM when the mass is $m \sim 10^{-23} - 10^{-22}$ eV [11, 37]. Such an extraordinarily light particle is considered an axion, and it is a candidate for DM [38]. Such DM can interact with each other because some observations of galaxy cluster collisions indicate that the DM has a non-negligible scattering cross section *i.e.*, self-interaction [39, 40].

The scalar field DM model implies that the DM halos become BECs. If scalar bosons describe the DM in this model, the boson has a galaxy-scale de Broglie wavelength of the order of 1 kpc [28, 41]. Then, the DM halo obtains a high critical temperature for Bose-Einstein condensation in the order of 10^9 K [42–44]. This temperature is significantly higher than the present background temperature 2.7 K [44]. Thus, the halo can be considered a BEC. If DM halos are BECs, self-interaction is

* sn22896p@st.omu.ac.jp

† h.ishihara@omu.ac.jp

‡ tsubota@omu.ac.jp

introduced into the GP model. The competition between gravity and self-interactions forms the configuration of a halo. Such a BEC is defined as a self-gravitating BEC that follows the Gross-Pitaevskii-Poisson (GPP) equation [11, 13, 14].

Various properties of DM halos have been studied theoretically using the GPP equation in recent astrophysics studies. Böhmer and Harko used the Thomas-Fermi (TF) approximation to compare their model predictions with the observational data on the rotational motion of galaxies [15]. Subsequently, many studies using the approximation have appeared, including the divergence of the central density of the CDM model called the core-cusp problem [45], gravitational lensing effects [46], deformation by rotation [42], and the effects of quantized vortices [16, 47]. The variational method has also been applied to the GPP equation to investigate the relationship between the total mass and radius of self-gravitating BECs [13], gravitational collapse [48, 49], and the phase transition between dilute and dense phases [50]. There were analyses of gravitational instability, Jeans instability [51–53], and the effects of vortex lattices [43]. Furthermore, numerical studies on self-gravitating BECs have recently been reported. The stability of the equilibrium state [54] and the stabilization process [55] were investigated by numerically solving the GPP equation. The rotational velocity of a test particle in a self-gravitating BEC was studied in [17, 56]. When self-gravitating BECs are close together, they can collide [57] because of gravity. Thus far, numerical studies have typically imposed spatial symmetry on the system in order to reduce computational costs. However, recent numerical studies used a three-dimensional system without spatial symmetry. Such studies focused on quantized vortices in self-gravitating BECs, such as the stability [18, 58] and the collision of self-gravitating BECs with quantized vortices [59].

Self-gravitating BECs differ from atomic BECs in their trapping potential. In low temperature physics, the BEC is generally trapped by external potentials. The external potential is prescribed independently of the configuration of BEC. Thus, the BEC does not affect the trapping potential, regardless of how much it moves. However, a self-gravitating BEC is trapped by its own gravitational potential, even without any external potential. In addition, the deformation of the BEC can change the strength, range, and anisotropy of the gravitational potential. Such differences between self-gravitating BECs and atomic BECs are important when we consider quantum fluids as candidates for astrophysical objects because they cause quantum hydrodynamical phenomena under self-gravity.

The collective mode is a phenomenon that the anisotropy of the trapping potential affects. This phenomenon is a low-frequency oscillation of a trapped BEC in response to small fluctuations. It can be described by representative variables as a one-body motion, despite being a many-body system. For example, the spherical

oscillation of a spherically trapped BEC, called breathing mode, is characterized by its radius *i.e.* the equation of motion for the radius is obtained using the GP equation [2]. One of the most important characteristics is that the collective modes depend on the shape of the trapping potential; considering the axisymmetric potential, the breathing and quadrupole modes are coupled [2]. Because the gravitational potential of self-gravitating BECs transforms with the oscillation of the BEC, the collective modes of self-gravitating BECs can exhibit behaviors quite different from the usual ones.

In this work, we study the three-dimensional dynamics of the collective modes of a self-gravitating BEC. We consider the total mass to be sufficiently large that a TF approximation is available. We prepare the initial state by multiplying the factor on the initial velocity with the equilibrium solution of the GPP equation and implement time evolution by numerically solving the GPP equation. First, the breathing mode of the self-gravitating BECs is induced by radially adding the initial velocity. Our numerical results agree with the analytical results obtained using the variational method. Next, by adding the initial velocity axisymmetrically, we numerically obtain the anisotropic collective mode in which the quadrupole mode is mixed with the breathing mode.

This paper is organized as follows. Our model and numerical setup are described in Sec.II. Based on this, the breathing mode of a self-gravitating BEC is studied in Sec.III. Anisotropic collective mode under self-gravity of the BEC is investigated in Sec.IV. Finally, we conclude this paper in Sec.V.

II. MODEL AND NUMERICAL SETUP

A. GROSS-PITAEVSKII-POISSON MODEL AND THE EQUILIBRIUM STATE

We consider that a self-gravitating BEC consisted of scalar bosons with mass m and an s-wave scattering length a at zero temperature. In the GPP model, the physical state of the BEC is described by the macroscopic wavefunction $\psi(\mathbf{r}, t)$ and the time evolution is given by the GPP equation:

$$\begin{cases} i\hbar\partial_t\psi = -\frac{\hbar^2}{2m}\nabla^2\psi + [mV + \frac{4\pi\hbar^2 a}{m}|\psi|^2]\psi, \\ \nabla^2 V = 4\pi m G |\psi|^2, \end{cases} \quad (1)$$

where $V(\mathbf{r}, t)$ denotes the gravitational potential [11, 13, 29]. Using the Madelung representation

$$\psi(\mathbf{r}, t) = \sqrt{\frac{\rho(\mathbf{r}, t)}{m}} e^{i\theta(\mathbf{r}, t)}, \quad (2)$$

the GP equation becomes the continuity equation and the Euler-like equation, where $\rho = m|\psi|^2$ denotes the density and $\mathbf{v} = \hbar\nabla\theta/m$ denotes the velocity field [2].

Then, the total mass is

$$M = \int d\mathbf{r} \rho(\mathbf{r}) = m \int d\mathbf{r} |\psi|^2. \quad (3)$$

The total energy E is the sum of these energies:

$$E = K + W + I, \quad (4)$$

$$K = \frac{\hbar^2}{2m} \int d\mathbf{r} |\nabla \psi|^2, \quad (5)$$

$$W = \frac{m}{2} \int d\mathbf{r} |\psi|^2 V, \quad (6)$$

$$I = \frac{2\pi\hbar^2 a}{m} \int d\mathbf{r} |\psi|^4, \quad (7)$$

where K denotes the kinetic energy, W denotes the potential energy, and I denotes the self-interaction energy [16].

We can obtain the equilibrium solution of the GPP equation (1) using the TF approximation [15]. When the kinetic energy is neglected *i.e.*, $K \ll I$, the configuration of the equilibrium state is formed by the competition between gravity and self-interaction [2]. The kinetic energy is negligible when the total mass is sufficiently large [52]. The equilibrium configuration should be spherically symmetrical under self-gravity. Assuming that the equilibrium state satisfies the ansatz $\psi(\mathbf{r}, t) = \phi(r)e^{-i\mu t/\hbar}$, the steady solution of Eq. (1) is approximately

$$\begin{aligned} \rho(r) &\simeq \rho_c j_0(\pi r/R_{\text{TF}}) \\ &= \rho_c \frac{\sin(\pi r/R_{\text{TF}})}{(\pi r/R_{\text{TF}})} \quad (r < R_{\text{TF}}), \end{aligned} \quad (8)$$

where $r = |\mathbf{r}|$ is the radial coordinate, μ is the chemical potential, ρ_c is the central density, and j_0 is the 0-th spherical Bessel function. Subsequently, the TF radius R_{TF} is defined as the minimum radius at which the density becomes zero:

$$R_{\text{TF}} = \pi \sqrt{\frac{\hbar^2 a}{Gm^3}}, \quad (9)$$

which implies that the size of a massive self-gravitating BEC does not depend on its total mass. There are no densities in the range of $r > R_{\text{TF}}$. Thus, the cumulative mass profile is

$$M(r) = \begin{cases} \frac{M_{\text{TF}}}{\pi} \left\{ \sin\left(\frac{\pi r}{R_{\text{TF}}}\right) - \frac{\pi r}{R_{\text{TF}}} \cos\left(\frac{\pi r}{R_{\text{TF}}}\right) \right\} & (r < R_{\text{TF}}), \\ M_{\text{TF}} & (r > R_{\text{TF}}), \end{cases} \quad (10)$$

where M_{TF} denotes

$$M_{\text{TF}} = \frac{4\rho_c R_{\text{TF}}^3}{\pi}. \quad (11)$$

Since the TF radius is independent of the total mass, Eq. (11) shows that only the central density increases, even

when the total mass increases. By solving the Poisson equation, the gravitational potential becomes

$$\begin{aligned} V(r) &= G \int_{\infty}^r ds \frac{M(s)}{s^2} \\ &= \begin{cases} -\frac{GM_{\text{TF}}}{R_{\text{TF}}} \left\{ 1 + j_0\left(\frac{\pi r}{R_{\text{TF}}}\right) \right\} & (r < R_{\text{TF}}), \\ -\frac{GM_{\text{TF}}}{r} & (r > R_{\text{TF}}). \end{cases} \end{aligned} \quad (12)$$

Therefore, using Eqs. (5), (6), (7), (8), and (12), the energy of each equilibrium state is

$$K \simeq \frac{\pi \hbar^2 M_{\text{TF}}}{8 m^2 R_{\text{TF}}^2} \left\{ \text{Si}(\pi) - \pi + \int_0^{\Lambda\pi} dx \frac{x}{\sin x} \right\}, \quad (13)$$

$$W = -\frac{3}{4} \frac{GM_{\text{TF}}^2}{R_{\text{TF}}}, \quad (14)$$

$$I = \frac{\pi^2 \hbar^2 a M_{\text{TF}}^2}{4 m^3 R_{\text{TF}}^3}, \quad (15)$$

where $\text{Si}(x)$ is a sine integral and $\Lambda\pi (< \pi)$ is the cutoff to avoid the divergence of the integral for $\Lambda \rightarrow 1$. The value of Λ can be estimated using the ratio between the coherence length $\xi = \sqrt{m/(8\pi a \rho_c)}$ and the TF radius, such that $\Lambda \sim 1 - \xi/R_{\text{TF}}$.

B. NUMERICAL SETUP

The GPP equation (1) is reduced to the following dimensionless form:

$$\begin{cases} i\tilde{\partial}_t \tilde{\psi} = -\frac{1}{2} \tilde{\nabla}^2 \tilde{\psi} + [\tilde{V} - i\tilde{V}_s + \tilde{a}|\tilde{\psi}|^2] \tilde{\psi}, \\ \tilde{\nabla}^2 \tilde{V} = |\tilde{\psi}|^2, \end{cases} \quad (16)$$

where the tilde symbols represent the dimensionless variables. The dimensionless variables are defined by, $\tilde{\mathbf{r}} = \mathbf{r}(\tilde{\lambda}mc/\hbar)$, $\tilde{t} = t(\tilde{\lambda}^2 mc^2/\hbar)$, $\tilde{\psi} = \psi\{\sqrt{4\pi G\hbar}/(\sqrt{mc^2}\tilde{\lambda})\}$, $\tilde{V} = V/(\tilde{\lambda}^2 c^2)$, $\tilde{a} = a\{\tilde{\lambda}^2 c^2/(mG)\}$ [17]. The scale factor $\tilde{\lambda}$ can arrange the system size using the invariance of the equations for any value [?]. Then, the dimensionless total mass and energy are, $\tilde{M} = M\{4\pi Gm/(\tilde{\lambda}\hbar c)\}$ and $\tilde{E} = E\{8\pi Gm/(\hbar c^3 \tilde{\lambda}^3)\}$.

The boundary conditions should be considered when addressing Eq. (16). The GP equation is typically solved under periodic boundary conditions. However, the Poisson equation is inconsistent with the periodic boundary condition owing to the long-range interaction of gravity. To overcome this inconsistency, we propose a novel method.

The GP equation in Eq. (16) is computed using the fourth-order Runge-Kutta and pseudo-spectrum methods under periodic boundary conditions. To solve the Poisson equation, we use the finite difference and Jacobi methods at each time step [60]. Using the Jacobi method, the solution of the Poisson equation in Eq. (16)

is the equilibrium solution of the diffusion equation for the function $\tilde{V}'(\tilde{\mathbf{r}}, \tilde{t}; \tilde{s})$:

$$\frac{d\tilde{V}'}{d\tilde{s}}(\tilde{\mathbf{r}}, \tilde{t}; \tilde{s}) = \tilde{\nabla}^2 \tilde{V}'(\tilde{\mathbf{r}}, \tilde{t}; \tilde{s}) - |\tilde{\psi}(\tilde{\mathbf{r}}, \tilde{t})|^2, \quad (17)$$

where \tilde{s} denotes a real parameter. The gravitational potential is obtained from $\tilde{V}(\tilde{\mathbf{r}}, \tilde{t}) = \lim_{\tilde{s} \rightarrow \infty} \tilde{V}'(\tilde{\mathbf{r}}, \tilde{t}; \tilde{s})$. Furthermore, the Jacobi method can be dramatically improved by Nesterov's accelerated gradient method [61–63]. This method is common in the field of machine learning and enables us to rapidly obtain the function $\tilde{V}'(\tilde{\mathbf{r}}, \tilde{t}; \tilde{s})$ optimized by Eq. (17). The function $\tilde{V}'(\tilde{\mathbf{r}}, \tilde{t}; \tilde{s})$ satisfies the Dirichlet boundary condition:

$$\tilde{V}'(\tilde{\mathbf{r}} = \tilde{\mathbf{R}}_b, \tilde{t}; \tilde{s}) = -\frac{\tilde{M}}{4\pi|\tilde{\mathbf{R}}_b - \tilde{\mathbf{R}}_c|} \quad (18)$$

where $\tilde{\mathbf{R}}_b$ is the position on the boundary of the numerical domain and $\tilde{\mathbf{R}}_c$ is the center of the numerical domain. The boundary condition (18) is appropriate when the BEC is smaller than the numerical domain and located near its center.

In our numerical model, the imaginary potential $-i\tilde{V}_s$, called "sponge" potential, such as

$$\tilde{V}_s(\mathbf{r}) = \frac{\tilde{V}_o}{2} \left\{ 2 + \tanh\left(\frac{\tilde{r} - \tilde{r}_c}{\tilde{\delta}}\right) - \tanh\left(\frac{\tilde{r}_c}{\tilde{\delta}}\right) \right\} \quad (19)$$

is introduced into Eq. (16) [17]. \tilde{V}_o denotes the amplitude. This sponge potential can reduce the number of particles in the range of $\tilde{r} > \tilde{r}_c$, where $\tilde{\delta}$ is the step width. The sponge potential plays a role in removing particles emitted from the BEC. When the BEC moves, some particles obtain high kinetic energy and escape from the gravitational potential. However, in our system, they return to the BEC by a periodic boundary condition for the GP equation. In order to avoid the unphysical situation, we require the sponge potential.

The initial state is prepared by multiplying the factor of the initial phase $\exp[i\tilde{\phi}(\tilde{\mathbf{r}})]$ to the equilibrium state $\tilde{\psi}_{\text{eq}}(\tilde{\mathbf{r}})$:

$$\tilde{\psi}(\tilde{\mathbf{r}}, \tilde{t} = 0) = \tilde{\psi}_{\text{eq}}(\tilde{\mathbf{r}}) e^{i\tilde{\phi}(\tilde{\mathbf{r}})}. \quad (20)$$

The BEC is located at the center of the numerical domain. The equilibrium state $\tilde{\psi}_{\text{eq}}$ is obtained using the imaginary time propagation method of the GPP equation. The initial phase is given by

$$\tilde{\phi}(\tilde{r}_\perp, \tilde{z}) = \frac{1}{2} \left(\tilde{\alpha} \tilde{r}_\perp^2 + \tilde{\beta} \tilde{z}^2 \right), \quad (21)$$

which yields the initial velocity field $\tilde{\mathbf{v}} = \tilde{\nabla} \tilde{\phi} = (\tilde{\alpha} \tilde{r}_\perp) \mathbf{e}_\perp + (\tilde{\beta} \tilde{z}) \mathbf{e}_z$. Here, $\tilde{r}_\perp = \sqrt{\tilde{x}^2 + \tilde{y}^2}$ and \tilde{z} are the 3D cylindrical coordinates, and the unit vectors along each direction are \mathbf{e}_\perp and \mathbf{e}_z . We determine the initial velocity by $\tilde{\alpha}$ and $\tilde{\beta}$ (e.g., it becomes isotropic when $\tilde{\alpha} = \tilde{\beta}$).

Finally, the physical and numerical parameters are denoted. We consider that each boson has a mass $m = 3 \times 10^{-24}$ eV and an s-wave scattering length $a = 5.62 \times 10^{-98} \lambda_c$ m, where λ_c is the Compton wavelength [18]. For the numerical analyses, we use a 3D cube of length $\tilde{L}_x = \tilde{L}_y = \tilde{L}_z = 40$. The scale factor is $\tilde{\lambda} = 3 \times 10^{-3}$, such that the numerical domain is much larger than the BEC. The spatial grid is set to $\tilde{N}_x = \tilde{N}_y = \tilde{N}_z = 128$. The time resolution of the GP equation is $\Delta \tilde{t} = 10^{-3}$ and the resolution of the parameter \tilde{s} is $0.05 \times (\tilde{L}_x / \tilde{N}_x)^2 \approx 4.88 \times 10^{-3}$. The parameters of the sponge potential are $\tilde{V}_o = 1000$, $\tilde{r}_c = 0.8 \times (\tilde{L}_x / 2) = 16$ and $\tilde{\delta} = 2 \times (\tilde{L}_x / \tilde{N}_x) = 0.625$. Then, \tilde{r}_c is larger than the dimensionless TF radius $\tilde{R}_{\text{TF}} \approx 9.09$, which is the typical size of a BEC. This is reasonable because the sponge potential works outside the BEC. In all our simulations, the particles are hardly emitted from the BEC.

III. BREATHING MODE

In this section, we consider the breathing modes of self-gravitating BEC. In the case of a typical BEC trapped by an external potential, the initial radial velocity field induces the breathing mode [2, 20, 64]. Similarly, we analytically and numerically study the breathing mode of a self-gravitating BEC by setting a spherically symmetric initial phase. Our numerical results are verified by comparing them with our analytical calculations.

A. ANALYTICAL CALCULATION BY VARIATIONAL METHOD

We apply the variational method to the GPP model to describe the breathing modes of self-gravitating BECs. We consider a self-gravitating BEC with a fixed total mass M . Previous studies used Gaussian [13] and quadratic functions [48] as the trial functions of the variational method. We adopt the 0-th spherical Bessel function as the trial function because we consider that the self-gravitating BEC have a large total mass, allowing us to use the TF approximation. This approach is the most appropriate for such a large total mass.

We prepare a trial function for applying the variational method. When the self-gravitating BEC is large that the TF approximation is available, the macroscopic wavefunction of the equilibrium state is obtained as

$$\psi_{\text{eq}}(r) = \sqrt{\frac{\pi M}{4mR_{\text{TF}}^3}} j_0 \left(\frac{\pi r}{R_{\text{TF}}} \right) \quad (22)$$

using Eqs. (8) and (11). Assuming that the density profile maintains its form as in Eq. (22) during the motion of the cloud, the trial function can obtain

$$\psi(\mathbf{r}, t) = \sqrt{\frac{\pi M}{4mR(t)^3}} j_0 \left(\frac{\pi r}{R(t)} \right) \exp \left[i \frac{m r^2}{2\hbar} H(t) \right] \quad (23)$$

in the range of $r < R(t)$ [2, 48, 49]. Then, we can consider the radius $R(t)$ and $H(t)$ as variables of breathing mode.

We obtain the Euler-Lagrange equations for $R(t)$ and $H(t)$. The GPP model can be described by a Lagrangian

$$L = \frac{i\hbar}{2} \int d\mathbf{r} (\psi^* \partial_t \psi - \psi \partial_t \psi^*) - E, \quad (24)$$

using Eq. (4) [48]. Substituting the trial function (23), the Lagrangian becomes

$$L(R, H) = -\frac{1}{2} \left(1 - \frac{6}{\pi^2} \right) MR^2 (\dot{H} + H^2) - U(R). \quad (25)$$

Here, the effective potential $U(R)$ is

$$\begin{aligned} U(R) &= \frac{\pi}{8} \frac{\hbar^2 M}{m^2 R^2} F(\Lambda) - \frac{3}{4} \frac{GM^2}{R} + \frac{\pi^2}{4} \frac{\hbar^2 a M^2}{m^3 R^3} \\ &\equiv \frac{C_z}{R^2} - \frac{C_p}{R} + \frac{C_i}{R^3}. \end{aligned} \quad (26)$$

Here the coefficients are $C_z = \frac{\pi}{8} \frac{\hbar^2 M}{m^2} F(\Lambda)$, $C_p = \frac{3}{4} GM^2$, and $C_i = \frac{\pi^2}{4} \frac{\hbar^2 a M^2}{m^3}$, and the function $F(\Lambda) = \text{Si}(\pi) - \pi + \int_0^{\Lambda\pi} dx \frac{x}{\sin x}$. Hence, the Euler-Lagrange equation for $H(t)$ is $H(t) = \dot{R}(t)/R(t)$, and the radius $R(t)$ follows the equation:

$$\left(1 - \frac{6}{\pi^2} \right) M \frac{d^2 R(t)}{dt^2} = -\frac{dU(R)}{dR} \quad (27)$$

[?].

The equilibrium solution R_{eq} is obtained using $dU(R)/dR = 0$ as

$$\begin{aligned} R_{\text{eq}} &= \frac{C_z + \sqrt{C_z^2 + 3C_p C_i}}{C_p} \\ &= \frac{\pi^2 \hbar^2}{6Gm^2} \frac{F(\Lambda)}{M} \left\{ 1 + \sqrt{1 + \frac{36Gam}{\pi^2 \hbar^2} \frac{M^2}{F(\Lambda)^2}} \right\}. \end{aligned} \quad (28)$$

Fig. 1 describes the result of Eq. (28) when we set the cutoff parameter to $\Lambda = 0.97$. This figure shows that as the total mass M increases, R_{eq} decreases monotonically with gravity and converges to the TF radius of Eq. (9), for $M \rightarrow \infty$. Thus, our result can improve the relationship compared with previous studies [13, 48] using other trial functions when the total mass is large.

The breathing mode can be described as a small oscillation of radius around R_{eq} . The fluctuation is given by $R(t) = R_{\text{eq}} + \delta R(t)$ ($|\delta R(t)| \ll R_{\text{eq}}$). Using Eqs. (26), (27), and (28), we obtain the following equation of motion:

$$\begin{aligned} \frac{d^2 \delta R(t)}{dt^2} &\simeq -\frac{\pi^2}{\pi^2 - 6} \frac{1}{M} \frac{d^2 U(R_{\text{eq}})}{dR^2} \delta R(t) \\ &= -\frac{2\pi^2}{\pi^2 - 6} \frac{C_z R_{\text{eq}} + 3C_i}{MR_{\text{eq}}^5} \delta R(t). \end{aligned} \quad (29)$$

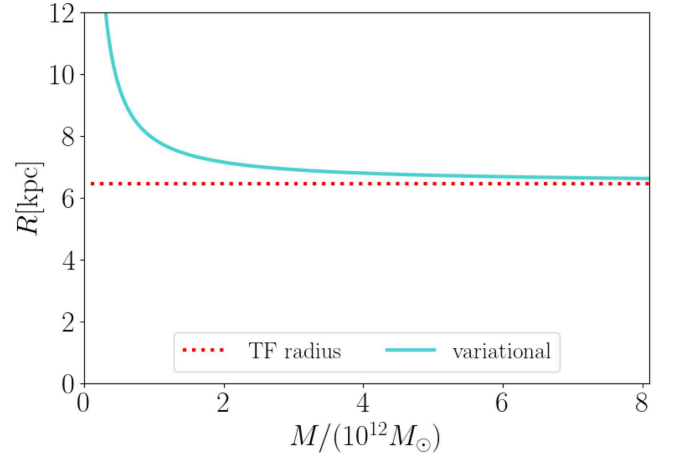


FIG. 1. The relation between the total mass M and the radius R derived by Eq. (9) when we set the cut-off parameter by $\Lambda = 0.97$. The horizontal axis shows the total mass, and the vertical axis shows the radius. The cyan solid line shows the analytical result of Eq. (9), and the red dotted line shows the TF radius R_{TF} .

Here, we consider the total mass of the BEC to be sufficiently large that the TF approximation is available. Because C_z is negligible, we can simplify Eq. (29) to

$$\frac{d^2 \delta R(t)}{dt^2} = -\frac{3}{2\pi(\pi^2 - 6)} \sqrt{\frac{G^5 m^9}{\hbar^6 a^3}} M \delta R(t), \quad (30)$$

which implies a harmonic oscillation with a period

$$T_B = 2\pi \sqrt{\frac{2\pi(\pi^2 - 6)}{3}} \sqrt{\frac{\hbar^6 a^3}{G^5 m^9}} \frac{1}{\sqrt{M}}. \quad (31)$$

The dependence on M was also reported in previous studies [13, 48]. The prefactor and M -dependence can be confirmed by the following numerical calculations.

B. NUMERICAL RESULTS

In order to conform Eq. (31), we perform numerical simulations for the total mass $M/(10^{14} M_\odot) = 1, 2, 3, 4$ with solar mass M_\odot . These values are much larger than typical values. For example, the Andromeda galaxy has $M \sim 10^{12} M_\odot$ [16] and the Milky Way has $M \simeq 0.5 - 2.0 \times 10^{12} M_\odot$ [65]. However, such a large total mass enables us to easily investigate the oscillation of the BEC because R_{eq} hardly change even if the total mass is reduced (see Fig 1). We set the parameters of the initial phase to $\tilde{\alpha} = \tilde{\beta} = \pm 0.03, 0.1$ to add isotropic velocity to the equilibrium state.

First, we describe the time evolution of the density and gravitational potential profiles. In the simulations presented in this section, although the fully three-dimensional GPP equation is solved, the configurations of the BECs maintain spherical symmetry during the time

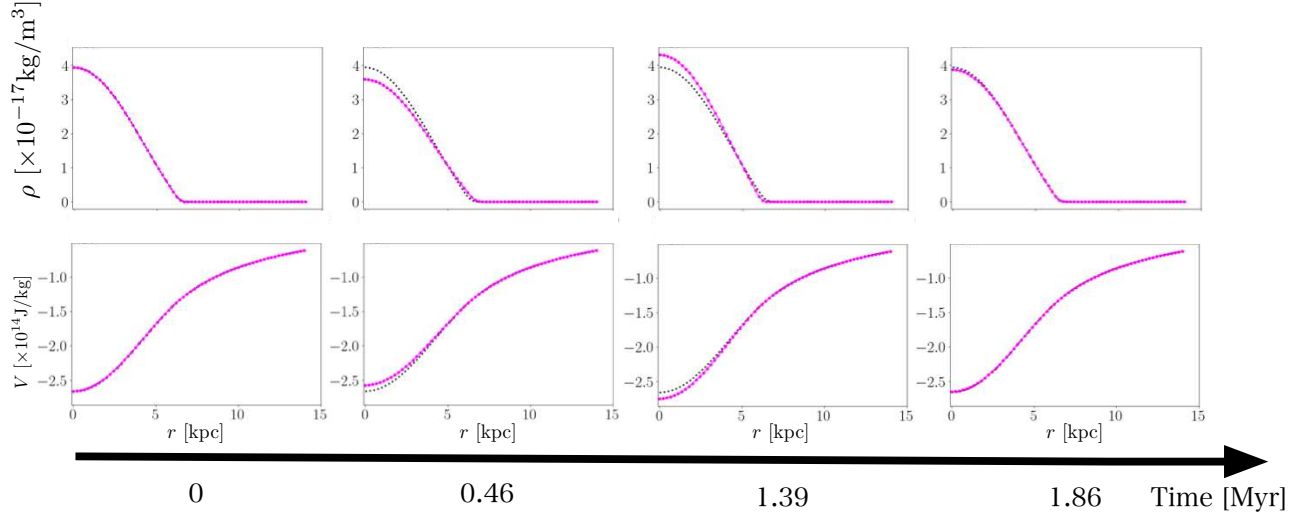


FIG. 2. The density profile and the gravitational potential of the self-gravitating BEC. The total mass is $M = 2 \times 10^{14} M_{\odot}$ and the initial phase is set by $\tilde{\alpha} = \tilde{\beta} = 0.1$. The horizontal axis shows the radial coordinate, which is defined as the distance from the center of our numerical domain. Each column is the density profile or the gravitational potential at each time: $t = 0, 0.46, 1.39, 1.86$ Myr, where Myr means a megayear. The magenta points show the data at each time, and the black dashed line shows the initial data. The upper row shows the density profile, and the vertical axis shows the density. The lower row shows the gravitational potential, and the vertical axis shows its value.

evolution. Then, we consider the average of the density and gravitational potential over the solid angle to describe the time evolution such that

$$\rho(r, t) = \frac{1}{4\pi r^2 \Delta r} \int_{r-\frac{\Delta r}{2}}^{r+\frac{\Delta r}{2}} dr' r'^2 \int d\Omega \rho(\mathbf{r}', t) \quad (32)$$

and

$$V(r, t) = \frac{1}{4\pi r^2 \Delta r} \int_{r-\frac{\Delta r}{2}}^{r+\frac{\Delta r}{2}} dr' r'^2 \int d\Omega V(\mathbf{r}', t), \quad (33)$$

where Ω denotes a solid angle. Fig. 2 shows the time evolution of the profiles of the density and gravitational potential. The BEC periodically undergo repeated spherical expansion and shrinkage. The BEC expands by adding the initial velocity directed outwards, and the central density decreases until $t = 0.46$ Myr. Subsequently, the BEC shrinks, and the central density increases until $t = 1.39$ Myr. Finally, the BEC returns to its initial state at $t = 1.86$ Myr. The gravitational potential also oscillates simultaneously with the density profile. The gravitational potential becomes shallow when the central density decreases, and vice versa. Note that at the outskirts, namely, for $r \gtrsim R_{\text{TF}} \approx 6.46$ kpc, the gravitational potential does not change during the time evolution, maintaining $V = -GM/r$ because the total mass is constant.

To observe the spherical oscillation quantitatively, we define the effective radius R_{eff} as

$$R_{\text{eff}}(t) = \sqrt{\frac{1}{M} \int dr r^2 \rho(r, t)}. \quad (34)$$

Using Eq. (23), it is proportional to the radius $R(t)$. Thus, when the self-gravitating BEC causes the breathing mode, the effective radius exhibits an oscillation similar to that of the radius. Figure 3(a) shows the change in effective radius from the initial value $\Delta R_{\text{eff}}(t) = R_{\text{eff}}(t) - R_{\text{eff}}(0)$ to $\tilde{\alpha} = 0.03$. The graph shows sinusoidal curves for each total mass. The oscillation can be characterized by the period $T_{R_{\text{eff}}}$ which decreases with M . Fig. 3(b) suggests that our results of $T_{R_{\text{eff}}}$ agree quantitatively with Eq. (31), even for three values of $\tilde{\alpha}$. Therefore, we determine that the self-gravitating BEC causes the breathing mode.

IV. APPEARANCE OF ANISOTROPIC MODE

A. NUMERICAL RESULTS

We consider the axisymmetric collective mode of a self-gravitating BEC. Its total mass is $M/(10^{14} M_{\odot}) = 1, 2, 3, 4$, same as that in breathing mode. We can simulate these situations by setting $(\tilde{\alpha}, \tilde{\beta}) = (\pm 0.03, 0), (0, \pm 0.03)$. Such parameters introduce a non-spherical initial velocity to the equilibrium state of the BEC and can cause anisotropic oscillation.

In order to describe the time evolution of the BEC, we obtain the density and gravitational potential profiles by averaging $\rho(\mathbf{r}, t)$ and $V(\mathbf{r}, t)$:

$$\rho(r_{\perp}, z, t) = \frac{1}{2\pi r_{\perp} \Delta r_{\perp}} \int_{r_{\perp}-\frac{\Delta r_{\perp}}{2}}^{r_{\perp}+\frac{\Delta r_{\perp}}{2}} dr'_{\perp} r'_{\perp} \int_0^{2\pi} d\theta \rho(r'_{\perp}, \theta, z, t) \quad (35)$$

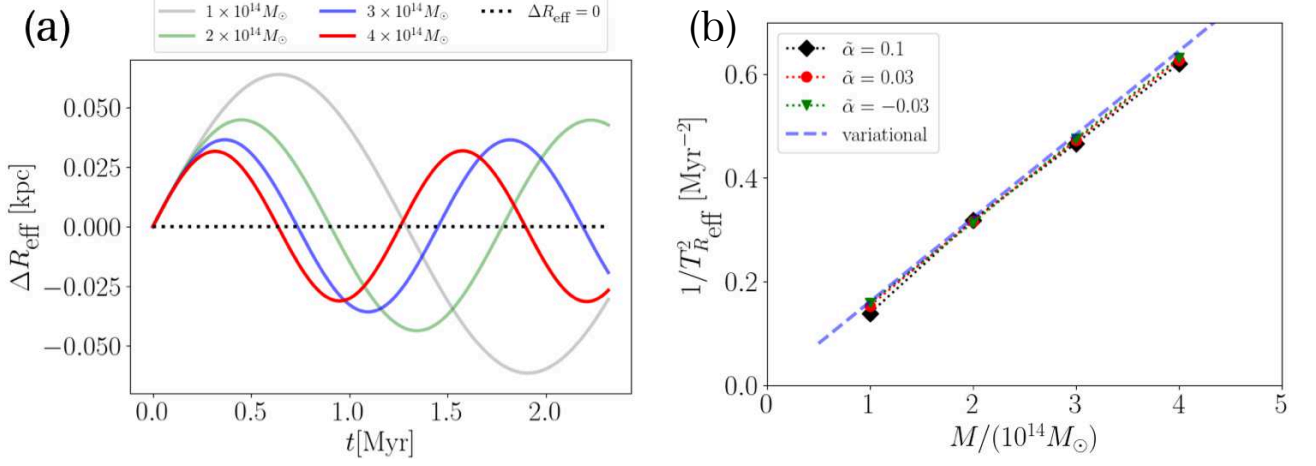


FIG. 3. Oscillation of the effective radius $R_{\text{eff}}(t)$ for each total mass of the self-gravitating BEC. (a) The change of the effective radius from the initial/equilibrium one $\Delta R_{\text{eff}}(t) = R_{\text{eff}}(t) - R_{\text{eff}}(0)$ when the initial phase is $\tilde{\alpha} = 0.03$. The horizontal axis shows the time, and the vertical axis shows $\Delta R_{\text{eff}}(t)$. Each solid curve is the time evolution of ΔR_{eff} for each total mass (red: $4 \times 10^{14} M_{\odot}$, blue: $3 \times 10^{14} M_{\odot}$, green: $2 \times 10^{14} M_{\odot}$ and black: $1 \times 10^{14} M_{\odot}$). The black dotted line shows the oscillation criterion, namely $\Delta R_{\text{eff}} = 0$. (b) Total mass dependency on the period of the effective radius $T_{R_{\text{eff}}}^{\text{eff}}$ for each value of $\tilde{\alpha}$. The horizontal axis shows the total mass, and the vertical axis shows the minus squared period $1/T_{R_{\text{eff}}}^2$. Each point shows the numerical result (black square: $\tilde{\alpha} = 0.1$, red solid circle: $\tilde{\alpha} = 0.03$ and green triangle: $\tilde{\alpha} = -0.03$). The blue dashed line shows the analytical result of the variational method *i.e.* the minus squared period of breathing mode $1/T_{\text{B}}^2$.

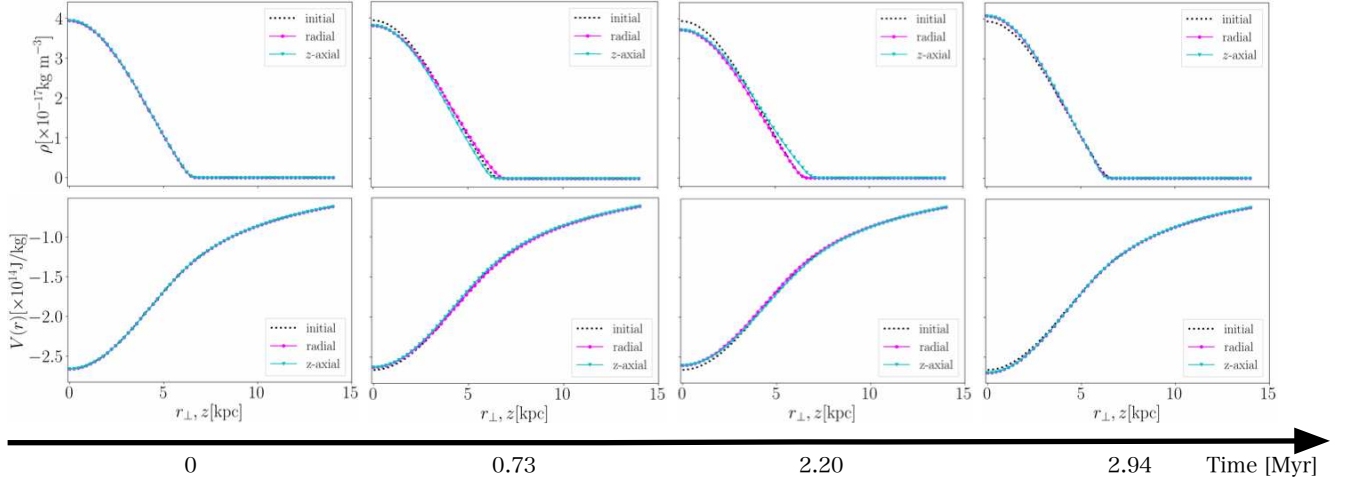


FIG. 4. The time evolution of the density profile $\rho(r_{\perp}, z)$ and the gravitational potential $V(r_{\perp}, z)$. We consider the BEC has the total mass $M = 2 \times 10^{14} M_{\odot}$ and is added the initial velocity by $\tilde{\alpha} = 0.1, \tilde{\beta} = 0$. The horizontal axis shows r_{\perp} and z . The magenta points show the profiles when $z = 0$, namely $\rho(r_{\perp}, z = 0)$ and $V(r_{\perp}, z = 0)$, and the cyan triangles show the ones when $r_{\perp} = 0$, namely $\rho(r_{\perp} = 0, z)$ and $V(r_{\perp} = 0, z)$. The black dashed lines show the initial profile. Each column shows the density profile or the gravitational potential at each time: $t = 0, 0.73, 2.20, 2.94$ Myr, where Myr means a megayear. The upper row shows the density profile, and the vertical axis shows the density. The lower row shows the gravitational potential, and the vertical axis shows its value.

and

$$V(r_{\perp}, z, t) = \frac{1}{2\pi r_{\perp} \Delta r_{\perp}} \int_{r_{\perp} - \frac{\Delta r_{\perp}}{2}}^{r_{\perp} + \frac{\Delta r_{\perp}}{2}} dr'_{\perp} r'_{\perp} \int_0^{2\pi} d\theta V(r'_{\perp}, \theta, z, t), \quad (36)$$

where $\theta = \tan^{-1}(y/x)$. Fig.4 shows the density profile and the gravitational potential. They show simultaneous oscillations similar to those in the breathing mode. How-

ever, $\rho(r_{\perp}, z = 0, t)$ is different from $\rho(r_{\perp} = 0, z, t)$. At $t = 0.73$ Myr, the former shows an expansion of the BEC, but the latter shows shrinkage compared to the initial one. Subsequently, the density profile at $t = 2.20$ Myr exhibits the opposite trend: a decrease in $\rho(r_{\perp}, z = 0, t)$ and an increase in $\rho(r_{\perp} = 0, z, t)$. At $t = 2.94$ Myr, the density profile returns to a spherical shape, similar to

the initial profile. Hence, the self-gravitating BEC causes anisotropic oscillations due to the nonspherical initial velocity. We observe this behavior for other combinations of $(\tilde{\alpha}, \tilde{\beta})$ such as $\tilde{\alpha} \neq \tilde{\beta}$ (e.g. $(\tilde{\alpha}, \tilde{\beta}) = (\pm 0.1, \mp 0.03)$).

To extract the effective degrees of freedom from the anisotropic oscillation, we introduce two quantities R_{eff}^{\perp} and Z_{eff} :

$$R_{\text{eff}}^{\perp}(t) = \sqrt{\frac{1}{M} \int d\mathbf{r} r_{\perp}^2 \rho(\mathbf{r}, t)}, \quad (37)$$

$$Z_{\text{eff}}(t) = \sqrt{\frac{1}{M} \int d\mathbf{r} z^2 \rho(\mathbf{r}, t)}. \quad (38)$$

These are the effective widths of the BEC in each direction; R_{eff}^{\perp} is the width in the direction of the radial coordinate r_{\perp} and Z_{eff} is the width in the direction of the z -axis. Fig. 5 shows the complicated oscillation of these quantities. The figure describes the opposite oscillation between R_{eff}^{\perp} and Z_{eff} . The BEC causes shrinkage in the direction of the z -axis when we initially provide a positive velocity in the direction of r_{\perp} , and vice versa. Similarly, the BEC shows shrinkage in the direction of r_{\perp} in response to the positive initial velocity in the direction of the z -axis, and vice versa.

Although R_{eff}^{\perp} and Z_{eff} exhibit complex oscillations, a harmonic oscillation can be obtained from the ratio $Z_{\text{eff}}/R_{\text{eff}}^{\perp}$, as shown in Fig. 6. Among the four cases, the oscillations has a common amplitude and frequency despite the different behaviors of R_{eff}^{\perp} , Z_{eff} . The ratio $Z_{\text{eff}}/R_{\text{eff}}^{\perp}$ indicates the extent to which the BEC is axisymmetrically deformed from a spherical shape, similar to the aspect ratio of the BEC. We can predict that one of the coupled modes is the quadrupole mode because the harmonic mode of the aspect ratio suggests a quadrupole mode of the BEC [66–68].

The Fourier transformation is useful for decomposing complicated oscillations into eigenmodes. Fig. 7 shows the Fourier transformation of R_{eff}^{\perp} and $Z_{\text{eff}}/R_{\text{eff}}^{\perp}$ shown in Fig. 5 and Fig. 6. We can find two peaks of R_{eff}^{\perp} and a peak of $Z_{\text{eff}}/R_{\text{eff}}^{\perp}$. The high-frequency peak of R_{eff}^{\perp} corresponds to the breathing mode T_B of the BEC with the same total mass. On the other hand, the low-frequency peak of R_{eff}^{\perp} is similar to that of $Z_{\text{eff}}/R_{\text{eff}}^{\perp}$. This peak suggests the frequency of the quadrupole mode of the BEC. Therefore, the self-gravitating BEC causes an anisotropic collective mode in which the quadrupole mode superposes the breathing mode by the axisymmetric initial velocity.

Finally, we change the parameters of the initial phase and total mass to investigate the dependence of the period of $Z_{\text{eff}}/R_{\text{eff}}^{\perp}$ on these quantities. Although we study the dynamics of some combinations of $\tilde{\alpha}$ and $\tilde{\beta}$, the period is constant for all the simulations. Hence, the period $Z_{\text{eff}}/R_{\text{eff}}^{\perp}$ is independent of the initial velocity. However, the total mass can change the period of $Z_{\text{eff}}/R_{\text{eff}}^{\perp}$, as shown in Fig. 8. Fig. 8 (a) shows that $Z_{\text{eff}}/R_{\text{eff}}^{\perp}$ exhibits the harmonic oscillation similar to R_{eff}^{\perp} of the

breathing mode by the isotropic initial velocity; the period become short as the total mass increases. The M -dependence of the period of $Z_{\text{eff}}/R_{\text{eff}}^{\perp}$ and a comparison with T_B are shown in Fig. 8 (b). We find that $Z_{\text{eff}}/R_{\text{eff}}^{\perp}$ clearly shows a straight line parallel to T_B in the log-log plot, suggesting that the period of the quadrupole mode is also inversely proportional to \sqrt{M} , similar to the breathing mode. However, the period of $Z_{\text{eff}}/R_{\text{eff}}^{\perp}$ is approximately 1.57 times larger than T_B ; the quadrupole mode is, in other words, the lower frequency oscillation than the breathing mode. This property can be observed in atomic BECs trapped by an isotropic harmonic potential. The frequency of the breathing mode is $\sqrt{5/2}$ times as large as that of the quadrupole mode [20]. Hence, our numerical results are consistent with those of typical atomic BECs trapped by external potentials. The ratio of the period of $Z_{\text{eff}}/R_{\text{eff}}^{\perp}$ to T_B is close to that of the BEC trapped by an isotropic harmonic potential. Moreover, the periods of $Z_{\text{eff}}/R_{\text{eff}}^{\perp}$ are in good agreement with $\sqrt{5/2}T_B$ (see Fig. 8). Thus, the numerical results indicate that the quadrupole mode has the period $\sqrt{5/2}T_B$. In order to reproduce our numerical results, we extend the variational method of the spherical self-gravitating BEC in Sec. III-A to the axisymmetric system in the following subsection.

B. ANALYSIS OF AXISYMMETRIC COLLECTIVE MODE BY VARIATIONAL METHOD

Rindler-Daller and Shapiro extended the TF solution to an ellipsoidal self-gravitating BEC [11, 47] using the ellipsoidal approximation proposed by Lai *et al.* [69]. Considering that the self-gravitating BEC takes a spheroidal configuration with semi-axes R_{\perp} and Z , the extended TF solution is written as

$$\rho(q) = \frac{\pi M}{4R_{\perp}^2} j_0 \left(\frac{\pi q}{R_{\perp}} \right), \quad (39)$$

where M is the total mass and $q \in (0, R_{\perp}]$ satisfies $(q/R_{\perp})^2 = (r_{\perp}/R_{\perp})^2 + (z/Z)^2$. To obtain the density profiles in Eq. (39), the trial function is set as

$$\psi(\mathbf{r}, t) = \sqrt{\frac{\pi M}{4mR_{\perp}(t)^2 Z(t)}} j_0 \left(\frac{\pi q}{R_{\perp}(t)} \right) \times \exp \left[i \frac{m}{2\hbar} (r_{\perp}^2 H_{\perp}(t) + z^2 H_z(t)) \right], \quad (40)$$

where $H_{\perp}(t)$ and $H_z(t)$ are variables that provide the velocity field such that

$$\mathbf{v} = (r_{\perp} H_{\perp}(t)) \mathbf{e}_{\perp} + (z H_z(t)) \mathbf{e}_z. \quad (41)$$

The Lagrangian can be obtained by substituting Eq. (40) to its definition (24). Using Eq. (40), the energy components K , W , I defined by Eqs. (5), (6), and (7)

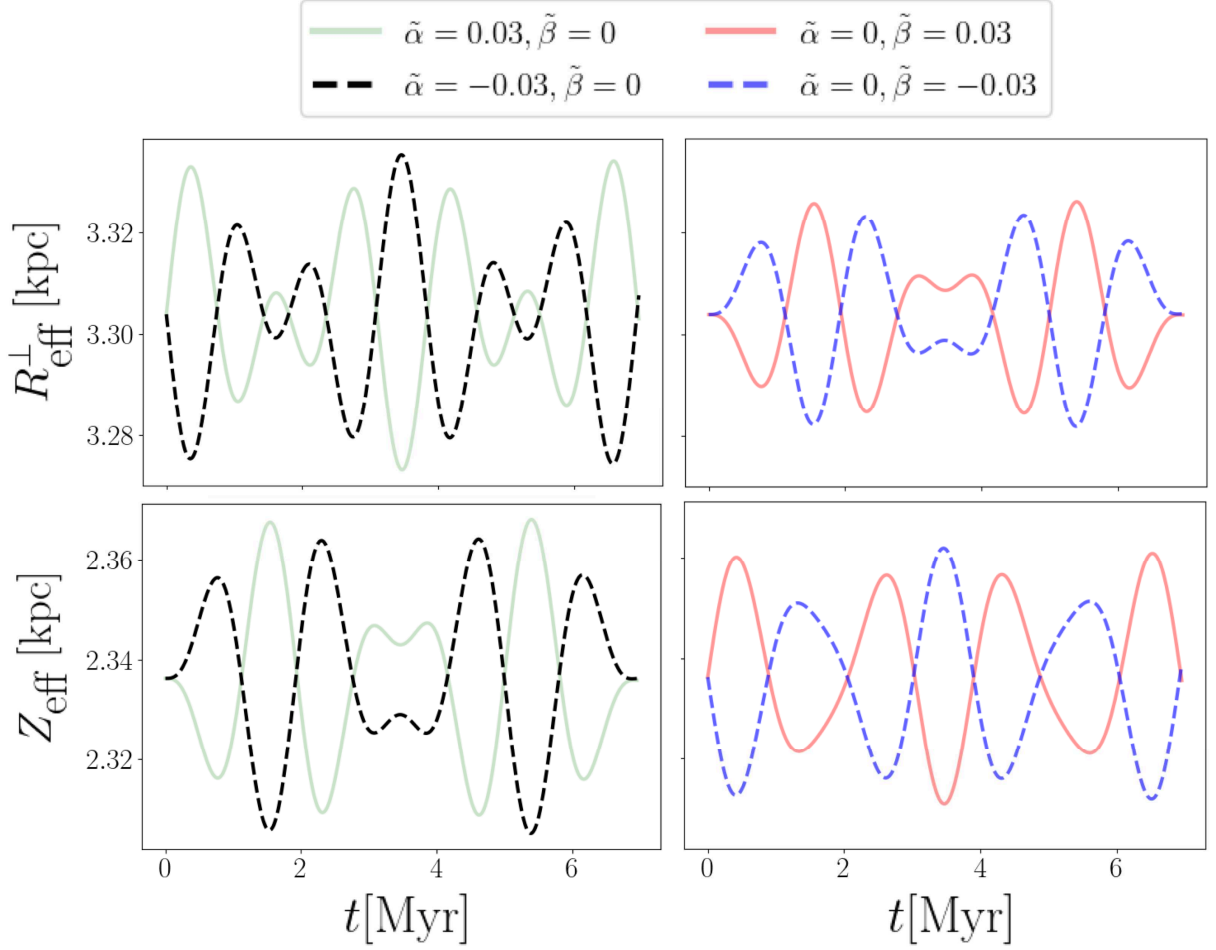


FIG. 5. Oscillations of the effective width R_{eff}^{\perp} , Z_{eff} . The self-gravitating BEC has the total mass $M = 4 \times 10^{14} M_{\odot}$ and the initial velocity is set by $(\tilde{\alpha}, \tilde{\beta}) = (\pm 0.03, 0)$, $(0, \pm 0.03)$. The vertical axis shows the time. The left column shows the result of $(\tilde{\alpha}, \tilde{\beta}) = (\pm 0.03, 0)$, which means the initial velocity in the direction of r_{\perp} . The green solid line shows the oscillation when the BEC initially expands ($\tilde{\alpha} > 0$), and the black broken line shows the oscillation when the BEC initially shrinks ($\tilde{\alpha} < 0$). On the other hand, the right column shows the result of $(\tilde{\alpha}, \tilde{\beta}) = (0, \pm 0.03)$, which means the initial velocity in the direction of the z -axis. The red solid line shows the oscillation when the BEC initially expands ($\tilde{\beta} > 0$), and the blue broken line shows the BEC initially shrinks ($\tilde{\beta} < 0$). While the upper row shows the time evolution of R_{eff}^{\perp} , the lower row shows the time evolution of Z_{eff} .

are

$$K \simeq \frac{\pi}{24} \frac{\hbar^2 M}{m^2} F(\Lambda) \left(\frac{2}{R_{\perp}(t)^2} + \frac{1}{Z(t)^2} \right) + \frac{M}{6} \frac{\pi^2 - 6}{\pi^2} \{ 2H_{\perp}(t)^2 R_{\perp}(t)^2 + H_z(t)^2 Z(t)^2 \} \quad (42)$$

$$W = -\frac{3GM^2}{4} \frac{1}{\{R_{\perp}(t)^2 Z(t)\}^{1/3}}, \quad (43)$$

$$I = \frac{\pi^2 \hbar^2 a M^2}{4} \frac{1}{m^3} \frac{1}{R_{\perp}(t)^2 Z(t)}, \quad (44)$$

where Eq. (43) can be derived using the formula for the gravitational energy of the spheroidal density profile in [33]. We assume that the deformation of the BEC is sufficiently small [?]. Hence, the Lagrangian can be

written as

$$L(R_{\perp}, Z, H_{\perp}, H_z) = -\frac{\pi^2 - 6}{6\pi^2} M \left\{ 2R_{\perp}^2 (\dot{H}_{\perp} + H_{\perp}^2) + Z^2 (\dot{H}_z + H_z^2) \right\} - U(R_{\perp}, Z). \quad (45)$$

Here, the effective potential $U(R_{\perp}, Z)$ is defined as

$$U(R_{\perp}, Z) = \frac{C_z}{3} \left(\frac{2}{R_{\perp}^2} + \frac{1}{Z^2} \right) - \frac{C_p}{(R_{\perp}^2 Z)^{1/3}} + \frac{C_i}{R_{\perp}^2 Z}, \quad (46)$$

where C_z , C_p and C_i are identical to those in Eq. (26). The Euler-Lagrange equations for $H_{\perp}(t)$ and $H_z(t)$ are $H_{\perp}(t) = \dot{R}_{\perp}(t)/R_{\perp}(t)$ and $H_z(t) = \dot{Z}(t)/Z(t)$. Therefore, the Euler-Lagrange equations for $R_{\perp}(t)$ and $Z(t)$

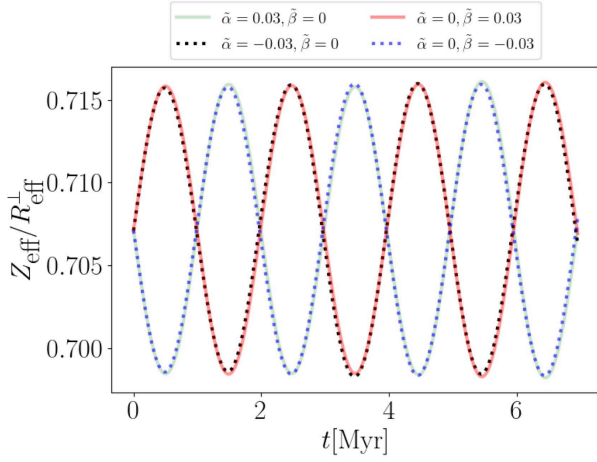


FIG. 6. The oscillation of the ratio $Z_{\text{eff}}/R_{\text{eff}}^{\perp}$ when the total mass of the self-gravitating BEC is $M = 4 \times 10^{14} M_{\odot}$. The horizontal axis shows the time, and the vertical axis shows the value of the ratio $Z_{\text{eff}}/R_{\text{eff}}^{\perp}$. The solid lines show the initially expanding cases (green: the direction of r_{\perp} and red: the direction of the z -axis), and the dotted lines show the initially shrinking cases (black: the direction of r_{\perp} and blue: the direction of the z -axis).

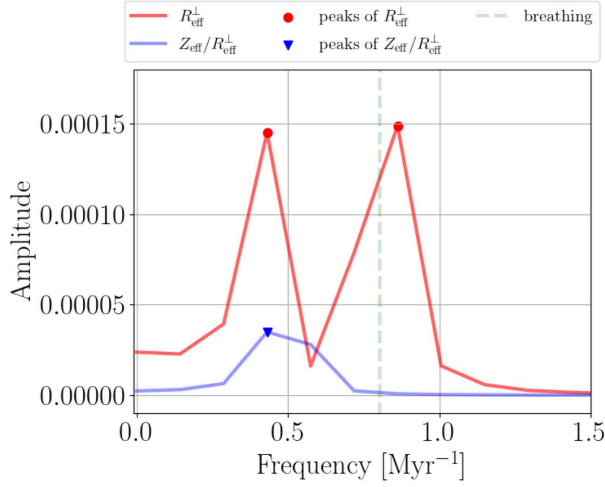


FIG. 7. The Fourier transform of R_{eff}^{\perp} and $Z_{\text{eff}}/R_{\text{eff}}^{\perp}$. The self-gravitating BEC has the total mass $M = 4 \times 10^{14} M_{\odot}$ and the initial velocity given by $\tilde{\alpha} = 0.03$, $\tilde{\beta} = 0$. The horizontal axis shows the frequency, and the vertical axis shows the amplitude. The solid lines show the results of each transformation (red: R_{eff}^{\perp} and blue: $Z_{\text{eff}}/R_{\text{eff}}^{\perp}$), and the green broken line shows the analytical/variational result of the breathing mode T_B . The red points show the peaks of R_{eff}^{\perp} , and the blue triangle shows the peak of $Z_{\text{eff}}/R_{\text{eff}}^{\perp}$.

are

$$\begin{cases} \frac{2}{3} \frac{\pi^2 - 6}{\pi^2} M \frac{d^2 R_{\perp}(t)}{dt^2} = - \frac{\partial U(R_{\perp}, Z)}{\partial R_{\perp}}, \\ \frac{1}{3} \frac{\pi^2 - 6}{\pi^2} M \frac{d^2 Z(t)}{dt^2} = - \frac{\partial U(R_{\perp}, Z)}{\partial Z}. \end{cases} \quad (47)$$

These Euler-Lagrange equations show the spherical equilibrium state with $R_{\perp} = Z = R_{\text{eq}}$, which is consistent with the results in Sec.III-A.

Similar to the spherically symmetric case, we consider a small oscillation of the semi-axes near R_{eq} . The fluctuations in the semi-axes are given by $R_{\perp}(t) = R_{\text{eq}} + \delta R_{\perp}(t)$ and $Z(t) = R_{\text{eq}} + \delta Z(t)$ ($|\delta R_{\perp}(t)|, |\delta Z(t)| \ll R_{\text{eq}}$). The equations of motion for the fluctuations $\delta R_{\perp}(t)$ and $\delta Z(t)$ are

$$\begin{aligned} & \frac{3(\pi^2 - 6)}{\pi^2} M R_{\text{eq}}^5 \frac{d^2}{dt^2} \begin{pmatrix} 2\delta R_{\perp}(t) \\ \delta Z(t) \end{pmatrix} \\ &= - \begin{pmatrix} 4C_p R_{\text{eq}}^2 & 2(-C_p R_{\text{eq}}^2 + 9C_i) \\ -C_p R_{\text{eq}}^2 + 9C_i & 5C_p R_{\text{eq}}^2 - 9C_i \end{pmatrix} \begin{pmatrix} 2\delta R_{\perp}(t) \\ \delta Z(t) \end{pmatrix}. \end{aligned} \quad (49)$$

If we write the solutions as $2\delta R_{\perp}(t) = A \exp[i\omega t]$ and $\delta Z(t) = B \exp[i\omega t]$, then the angular frequency ω satisfies

$$\omega = \pm \sqrt{\frac{2\pi^2}{\pi^2 - 6} \frac{C_z R_{\text{eq}} + 3C_i}{M R_{\text{eq}}^5}} \equiv \pm \omega_B, \quad (50)$$

or

$$\omega = \pm 2 \sqrt{\frac{\pi^2}{\pi^2 - 6} \frac{C_z}{M R_{\text{eq}}^4}} \equiv \pm \omega_Q. \quad (51)$$

Eq. (50) provides the eigenfrequency of the breathing mode compared to the coefficient of Eq. (29). Indeed, when $\omega = \pm \omega_B$, the eigenmodes satisfy $A = 2B$ *i.e.*

$$\begin{pmatrix} \delta R_{\perp}(t) \\ \delta Z(t) \end{pmatrix} = A \begin{pmatrix} 1 \\ 1 \end{pmatrix} \exp[\pm i\omega_B t]. \quad (52)$$

This indicates that the BEC either expands spherically or shrinks. On the other hand, when $\omega = \pm \omega_Q$, the eigenmodes satisfy $A + B = 0$ *i.e.*

$$\begin{pmatrix} \delta R_{\perp}(t) \\ \delta Z(t) \end{pmatrix} = A \begin{pmatrix} 1 \\ -2 \end{pmatrix} \exp[\pm i\omega_Q t]. \quad (53)$$

We can consider Eq. (53) as the quadrupole mode because it shows that the BEC is stretched along the z -axis or expanded along the xy -plane.

We compare Eqs. (52) and (53) with the numerical results. In our numerical simulations, we set two initial conditions: $\delta R_{\perp}(t=0) = \delta Z(t=0) = 0$ and $\tilde{\mathbf{v}}(\tilde{t}=0, \tilde{r}_{\perp}, \tilde{z}) = \tilde{\alpha} \tilde{r}_{\perp} \mathbf{e}_{\perp} + \tilde{\beta} \tilde{z} \mathbf{e}_z$. As a result, the fluctuations $\delta R_{\perp}(t)$ and $\delta Z(t)$ become

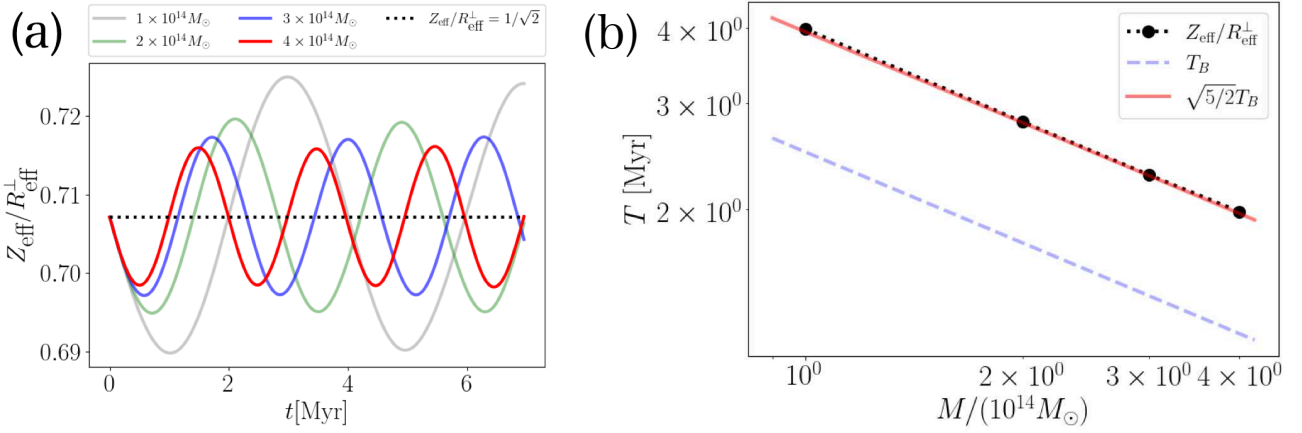


FIG. 8. The oscillation of $Z_{\text{eff}}/R_{\text{eff}}^{\perp}$ for each total mass. The initial phase is set by $\tilde{\alpha} = 0.03, \tilde{\beta} = 0$. (a) The time evolution of $Z_{\text{eff}}/R_{\text{eff}}^{\perp}$ for each total mass. The horizontal axis shows the time, and the vertical axis shows the value of $Z_{\text{eff}}/R_{\text{eff}}^{\perp}$. The black dotted line shows the ratio when the BEC is in the equilibrium state; the ratio becomes $Z_{\text{eff}}/R_{\text{eff}}^{\perp} = 1/\sqrt{2}$. Each solid line shows the result (red: $4 \times 10^{14} M_{\odot}$, blue: $3 \times 10^{14} M_{\odot}$, green: $2 \times 10^{14} M_{\odot}$, black: $1 \times 10^{14} M_{\odot}$). (b) The total mass dependence of $Z_{\text{eff}}/R_{\text{eff}}^{\perp}$ by the log-log plot. The horizontal axis shows the total mass, and the vertical axis shows the period. The black points show the numerical results for each total mass, while the blue broken line shows the variational result of the breathing mode T_B . The red solid line shows $\sqrt{5/2} T_B$.

$$\delta R_{\perp}(t) = \frac{\tilde{\lambda}^2 c^2 m R_{\text{eff}}}{3\hbar} \left\{ \frac{2\tilde{\alpha} + \tilde{\beta}}{\omega_B} \sin(\omega_B t) + \frac{\tilde{\alpha} - \tilde{\beta}}{\omega_Q} \sin(\omega_Q t) \right\}, \quad (54)$$

and

$$\delta Z(t) = \frac{\tilde{\lambda}^2 c^2 m R_{\text{eff}}}{3\hbar} \left\{ \frac{2\tilde{\alpha} + \tilde{\beta}}{\omega_B} \sin(\omega_B t) - 2 \frac{\tilde{\alpha} - \tilde{\beta}}{\omega_Q} \sin(\omega_Q t) \right\}. \quad (55)$$

The effective widths R_{eff}^{\perp} and Z_{eff} respectively result in $R_{\text{eff}}^{\perp} = \sqrt{2/3} \sqrt{(\pi^2 - 6)}/\pi^2 R_{\perp}$ and $Z_{\text{eff}} = \sqrt{(\pi^2 - 6)/(3\pi^2)} Z$ using Eq. (40). Thus we can find

$$\frac{Z_{\text{eff}}}{R_{\text{eff}}^{\perp}} = \frac{Z}{\sqrt{2} R_{\perp}} \simeq \frac{1}{\sqrt{2}} - \frac{\tilde{\lambda}^2 c^2 m (\tilde{\alpha} - \tilde{\beta})}{\sqrt{2} \hbar \omega_Q} \sin(\omega_Q t), \quad (56)$$

which show that the quadrupole mode causes a harmonic oscillation of $Z_{\text{eff}}/R_{\text{eff}}^{\perp}$ at near $1/\sqrt{2}$. This confirms that the quadrupole mode appears in the numerical simulations (Fig. 6 or Fig. 8 (a) in Sec. IV-A).

Our variational calculation of the axisymmetric self-gravitating BEC suggests that we can obtain only the quadrupole mode by selecting an appropriate initial phase. As the first term on the right-hand side of Eqs. (54) and (55) disappear, we can extract only the quadrupole mode by setting the initial phase as $2\tilde{\alpha} + \tilde{\beta} = 0$. Then, the quadrupole mode shows

$$\delta R_{\perp}(t) = \frac{\tilde{\alpha} \tilde{\lambda}^2 c^2 m R_{\text{eq}}}{\hbar \omega_Q} \sin(\omega_Q t) \quad (57)$$

and

$$\delta Z(t) = -2 \frac{\tilde{\alpha} \tilde{\lambda}^2 c^2 m R_{\text{eq}}}{\hbar \omega_Q} \sin(\omega_Q t), \quad (58)$$

which leads to harmonic oscillations of R_{eff}^{\perp} and Z_{eff} in the opposed phase. Indeed, we can numerically extract only the quadrupole mode when the total mass is $M = 4 \times 10^{14} M_{\odot}$ and the initial phase is set as $\tilde{\alpha} = 0.03$ and $\tilde{\beta} = -0.06$, as shown in Fig. 9. This figure shows that $\Delta R_{\text{eff}}^{\perp} \equiv R_{\text{eff}}^{\perp}(t) - R_{\text{eff}}^{\perp}(0)$ and $\Delta Z_{\text{eff}} \equiv Z_{\text{eff}}(t) - Z_{\text{eff}}(0)$ oscillate monotonically in the opposed-phase and their periods are the same as that shown in Fig. 6. Additionally, the amplitude of ΔZ_{eff} is approximately 1.40 times greater than that of $\Delta R_{\text{eff}}^{\perp}$, which is consistent with our analysis because Eqs. (57) and (58) predict that the ratio of the amplitudes of ΔZ_{eff} and $\Delta R_{\text{eff}}^{\perp}$ is $\sqrt{2}$. Therefore, we successfully extract only the quadrupole mode of self-gravitating BEC.

Although this variational method agrees qualitatively with the numerical results, the frequency or period of the quadrupole mode does not agree with them. The ratio of ω_Q to ω_B is

$$\frac{\omega_Q}{\omega_B} = 2 \sqrt{\frac{C_z R_{\text{eq}}}{C_p R_{\text{eq}}^2 + 3C_i}} \quad (59)$$

by Eqs. (28), (50) and (51). However, this ratio almost vanishes because we use $C_p R_{\text{eq}} \simeq 3C_i$ and $C_z R_{\text{eq}} \ll C_i$

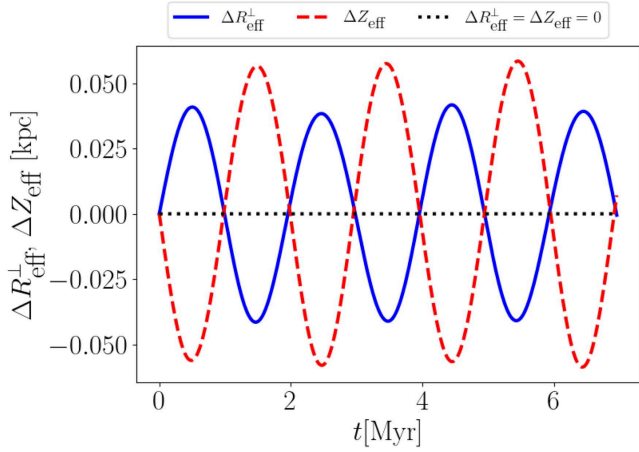


FIG. 9. The oscillation of the change of the effective widths $\Delta R_{\text{eff}}^{\perp} = R_{\text{eff}}^{\perp}(t) - R_{\text{eff}}^{\perp}(0)$ and $\Delta Z_{\text{eff}} = Z_{\text{eff}}(t) - Z_{\text{eff}}(0)$ when the total mass is $M = 4 \times 10^{14} M_{\odot}$ and the initial phase is set by $\tilde{\alpha} = 0.03$ and $\tilde{\beta} = -0.06$. The horizontal axis shows the time, and the vertical axis shows $\Delta R_{\text{eff}}^{\perp}$ and ΔZ_{eff} . The blue solid line shows the time evolution of $\Delta R_{\text{eff}}^{\perp}$, and the red broken line shows the time evolution of ΔZ_{eff} . The black dotted line shows that $\Delta R_{\text{eff}}^{\perp} = \Delta Z_{\text{eff}} = 0$.

in the TF approximation. This is clearly different from the numerical results that show that $\omega_Q/\omega_B = \sqrt{2/5}$ (see Fig. 8 (b)). This discrepancy is because the trial function in Eq. (40) is based on the TF solution. This approximation neglects the kinetic energy contribution and is broken near the surface of the BEC. However, Eqs. (13) and (51) show that the kinetic energy of the equilibrium state primarily determine the frequency of the quadrupole mode. Indeed, the quadrupole mode does not oscillate the central density, and neither the potential energy nor the self-interaction energy contributes to it. Consequently, the quadrupole mode can only change the BEC near the surface where the TF solution is broken down. Hence, a trial function based on the TF approximation does not allow us to quantitatively evaluate the contribution of the kinetic energy of the equilibrium state. This affects the frequency of the quadrupole mode. We must implement a first-order correction to the kinetic energy of the equilibrium state of the self-gravitating BEC to quantitatively compare ω_Q with the numerical results. This investigation will be conducted in a future study.

V. CONCLUSIONS

We study the collective modes of the self-gravitating BECs. In particular, we focus on breathing and anisotropic collective modes. In this study, we show the following three aspects.

A self-gravitating BEC can induce a breathing mode by adding an isotropic initial velocity to its equilibrium state. Because of the density dependence of self-gravity,

the gravitational potential near the center of the BEC oscillates with the density profile. The breathing mode of an ordinary BEC trapped by an external potential is characterized by the harmonic oscillation of the radius of the BEC, as similar to a self-gravitating BEC. However, as the total mass increases, the self-gravitating BEC reduces its amplitude and shortens its period. Moreover, the self-gravitating BEC indicates that the period of the breathing mode is inversely proportional to \sqrt{M} , which differs from an ordinal BEC trapped by a harmonic potential. This unique property clearly reflects the density dependence of self-gravity.

The axisymmetric initial velocity results in an anisotropic collective mode. It is found that the quadrupole mode is mixed with the breathing mode in the oscillation because the aspect ratio shows the harmonic oscillation for any choice of the initial velocity. The quadrupole mode also depends on the total mass. The amplitude and period decreases as the total mass increases, similar to the radius of the breathing mode. In addition, the period of the quadrupole mode has the same M -dependence as that of the breathing mode. Thus, it is inversely proportional to \sqrt{M} . This property is different from that of ordinary BECs trapped by an external potential. On the other hand, the ratio of the period of the quadrupole mode to that of the breathing mode is $\sqrt{5/2}$, as indicates by the BEC trapped by the isotropic harmonic potential.

We can extract only the quadrupole mode from the anisotropic collective mode by selecting an appropriate initial velocity. We extend the variational method, in which the trial function is based on the TF solution, to a spheroidal configuration. This result describes the anisotropic collective mode of the self-gravitating BEC and suggests the appropriate initial condition under which only the quadrupole mode occurs. We can numerically obtain the predicted results using the variational method. However, this variational method does not allow the evaluation of the kinetic energy of the equilibrium state. Consequently, it can not provide the proper frequency of the quadrupole mode because the frequency is determined by the contribution of the kinetic energy to the equilibrium state of the self-gravitating BEC. In order to quantitatively reproduce the frequency, we may have to implement a first-order correction of the kinetic energy.

When the oscillation has a large amplitude, the density dependence of the self-gravitating BEC probably changes the M -dependence of the periods and other characteristics of the collective mode. In this study, we consider the amplitude to be small. However, the large deformation of a self-gravitating BEC affects the gravitational energy. Considering the deformation, a collective mode with a large amplitude can cause some nontrivial phenomena (e.g., the emergence of differences in whether the spheroidal configuration is oblate or prolate).

Collective modes may occur when several BECs collide and merge. The oscillations are characterized by

eigenfrequency, which enable us to analyze the oscillation of the BEC after these phenomena. The existence of self-interaction is important because it determines the frequency, at least in the TF regime. In other words, we can observe the self-interaction effects of the self-gravitating BEC by the collective mode after the collision and merger.

We expect the collective modes of a self-gravitating BEC to be touchstones for the possibility that a dark matter halo is a BEC under self-gravity. In early studies on atomic BEC, its collective modes played a role in judging whether the system is a BEC. If Bose-Einstein condensation occurs and the BEC is formed in the universe, it is natural that the self-gravitating BEC exhibits such collective modes. In particular, anisotropic collective modes can emit the gravitational wave. Because the frequency of the collective mode of the self-gravitating BEC reflects the mass of the Bose particle and self-interaction, we can estimate these quantities from observations of the gravitational wave. Thus, this approach suggests a new method for identifying dark matter.

One of our interests is the collective mode of the rotating self-gravitating BEC. In the universe, an object is generally not at rest but rotates or oscillates, and dark matter halos are no exception. The equilibrium state

of a self-gravitating BEC is affected by rotation owing to its density dependence. For example, the quantized vortex in a BEC locally pushes the density through rotation, changing the density profile of the equilibrium state. Its gravitational potential is also different from that of a BEC without a quantized vortex. Hence, the self-gravitating BEC with a rotation or quantized vortex probably provides quite different phenomena of the collective modes from those in the present work.

ACKNOWLEDGMENTS

We thank M. Kobayashi and Y. Sano for their fruitful discussions of our numerical calculations. This work was supported by JST and the establishment of university fellowships for the creation of science and technology innovation, Grant Number JPMJFS2138. M. T. acknowledges the support from JSPS KAKENHI Grant Number JP23K03305. This study was partially supported by Osaka Central Advanced Mathematical Institute. MEXT Joint Usage/Research Center on Mathematics and Theoretical Physics, JPMXP0619217849.

-
- [1] A. J. Leggett, *Quantum Liquids Bose Condensation and Cooper Pairing in Condensed-Matter Systems*, (Oxford University Press 2006).
 - [2] C. J. Pethick and H. Smith, *Bose-Einstein Condensation in Dilute Gases*, second edition, (Cambridge University Press, 2008).
 - [3] G. E. Volovik, *The Universe in a Helium Droplet*, (Oxford University Press, 2003).
 - [4] T. W. B. Kibble, *J. Phys. Math. Gen.* **9**, 1387 (1976).
 - [5] W. H. Zurek, *Nature* **317**, 505 (1985).
 - [6] C. Bäuerle, Y. M. Bunkov, S. N. Fisher, H. Godfrin and G. R. Pickett, *Nature* **382**, 332 (1996).
 - [7] A. Keesling, A. Omran, H. Levine, H. Bernien, H. Pichler, S. Choi, R. Samajdar, S. Schwartz, P. Silvi, S. Sachdev, P. Zoller, M. Endres, M. Greiner, V. Vuletić and M. D. Lukin, *Nature* **568**, 207 (2019).
 - [8] W. G. Unruh, *Phys. Rev. Lett.*, **46**, 1351 (1981).
 - [9] M. Novello, M. Visser and G. Volovik, *ARTIFICIAL BLACK HOLES*, (World Scientific, 2002).
 - [10] I. Carusotto, S. Fagnocchi, A. Recati, R. Balbinot and A. Fabbri, *New J. Phys.*, **10**, 103001 (2008).
 - [11] C. M. González, J. E. M. Aguilar and L. M. R. Barrera, *Accelerated Cosmic Expansion : Proceedings of the Fourth International Meeting on Gravitation and Cosmology*, (Springer, 2013).
 - [12] J. Magaña and T. Matos, *J. Phys.: Conf. Ser.* **378**, 012012 (2012).
 - [13] P. H. Chavanis, *Phys. Rev. D* **84**, 043531(2011).
 - [14] P. H. Chavanis and L. Delfini, *Phys. Rev. D* **84**, 043532 (2011).
 - [15] C. G. Böhrer and T. Harko, *JCAP* **06**, 025(2007).
 - [16] B. Kain and H. Y. Ling, *Phys. Rev. D* **82**, 064042 (2010).
 - [17] F. S. Guzmán, F. D. Lora-Clavijo, J. J. González-Avilés and F. J. Rivera-Paleo, *Phys. Rev. D* **89**, 063507 (2014).
 - [18] Y. O. Nikolaieva, A. O. Olashyn, Y. I. Kuriatnikov, S. I. Vilchinskii and A. I. Yakimenko, *Low Temperature Physics* **47**, 684 (2021).
 - [19] A. L. Fetter, *Rev. Mod. Phys.* **81**, 647 (2009).
 - [20] L. Pitaevskii and S. Stringari, *Bose-Einstein Condensation*, (Oxford University Press, 2003).
 - [21] S. Inouye, M. R. Andrew, J. Stenger, H. -J. Miesner, D. M. Stamper-Kurn and W. Ketterle, *Nature* **392**, 151 (1998).
 - [22] E. P. Gross, *J. Math. Phys. Rev.* **4**, 195 (1963).
 - [23] L. P. Pitaevskii, *Sov. Phys. JETP* **13**, 451 (1961).
 - [24] I. Bloch, J. Dalibard and S. Nascimbène, *Nature phys.* **8**, 267 (2012).
 - [25] A. Sørensen, L. -M. Duan, J. I. Cirac and P. Zoller, *Nature* **409**, 63 (2001).
 - [26] M. C. Tsatsos, P. E. S. Tavares, A. Cidrim, A. R. Fritsch, M. A. Caracanhas, F. E. A. dos Santos, C. F. Barenghi and V. S. Bagnato, *Phys. Rep.* **622**, 1 (2016).
 - [27] M. Tsubota, M. Kobayashi and H. Takeuchi, *Phys. Rep.* **522**, 191 (2013).
 - [28] J. C. Niemeyer, *Progress in Particle and Nuclear Physics* **113**, 103787 (2020).
 - [29] E. G. M. Ferreira, *Astron. Astrophys. Rev.* **29**, 7 (2021).
 - [30] V. Rubin and W. Ford, *Astrophys. J.*, **159**, 379 (1970).
 - [31] A. Refregier, *Annu. Rev. Astron. Astrophys.* **41**, 645 (2003).
 - [32] K. Freese, *EAS*, **36**, 113 (2009).
 - [33] J. Binney and S. Tremaine, *GALACTIC DYNAMICS*, second edition, (Princeton University Press, 2008).
 - [34] A. D. Popolo and M. L. Delliou, *galaxies*, **5**, 1, 17 (2017).

- [35] A. Banerjee, K. K. Boddy, F. -Y. Cyr-Racine, A. L. Erickcek, D. Gilman, B. V. Lehmann, Y. -Y. Mao, P. Mocz, F. Munshi, E. O. Nadler, L. Necib, A. Parikh, A. H. G. Peter, L. Sales, M. Vogelsberger and A. C. Wright, arXiv:2203.07049 (2022).
- [36] W. Hu, R. Barkana and A. Gruzinov, Phys. Rev. Lett. **85**, 1158 (2000).
- [37] T. Matos and L. A. Ureña-López, Phys. Rev. D **63**, 063506(2001).
- [38] J. L. Feng, Annu. Rev. Astron. Astrophys., **48**, 495 (2010).
- [39] D. Harvey, R. Massey, T. Kitching, A. Taylor and E. Tittley, Science **347**, 1462 (2015).
- [40] M. Jauzac, D. Eckert, J. Schwinn, D. Harvey, C. M. Baugh, A. Rebertson, S. Bose, R. Massey, M. Owers, H. Ebeling, H. Y. Shan, E. Jullo, J. -P. Kneib, J. Richard, H. Atek, B. Clément, E. Egami, H. Israel, K. Knowles, M. Limousin, P. Natarajan, M. Rexroth, P. Taylor and C. Tchernin, Mon. Not. R. Astron. Soc. **463**, 3876 (2016).
- [41] L. Hui, J.P. Ostriker, S. Tremaine, E. Witten, Phys. Rev. D **95**, 043541 (2017).
- [42] X. Zhang, M. H. Chan, T. Harko, S. -D. Liang and C. S. Leung, Eur. Phys. J. C **78**, 346 (2018).
- [43] N. T. Zinner, Phys. Res. Int. **2011**, 734543 (2011).
- [44] M. P. Silverman and R. L. Mallett, General relativity and Gravitation **34**, 633 (2002).
- [45] T. Harko, J. Cosmol. Astropart. Phys. **05**, 022 (2011).
- [46] T. Harko and F. S. N. Lobo, Phys. Rev. D **92**, 043011 (2015).
- [47] T. Rindler-Daller and P. R. Shapiro, MNRAS **422**, 135 (2012).
- [48] T. Harko, Phys. Rev. D **89**, 084040 (2014).
- [49] P.-H. Chavanis, Phys. Rev. D **94**, 083007 (2016).
- [50] P.-H. Chavanis, Phys. Rev. D **98**, 023009 (2018).
- [51] A. Suárez and P. -H. Chavanis, Phys. Rev. D **98** 083529 (2018).
- [52] T. Harko, Eur. Phys. J. C **79**, 787 (2019).
- [53] P.-H. Chavanis, Universe **6**, 226 (2020).
- [54] F. S. Guzmán, F. D. Lora-Clavijo, J. J. González-Avilés and F. J. Rivera-Paleo, J. Cosmol. Astropart. Phys. **09**, 034 (2013).
- [55] F. S. Guzmán and L. A. Ureña-López, Astrophys. J. **645**, 814 (2006).
- [56] F. S. Guzmán, F. D. Lora-Clavijo, Gen. Relativ. Gravit. **47**, 21 (2015).
- [57] J. A. González and F. S. Guzmán, Phys. Rev. D **83**, 103513 (2011).
- [58] A. S. Dmitriev, D. G. Levkov, A. G. Panin, E. K. Pushnaya and I. I. Tkachev, Phys. Rev. D **104**, 023504 (2021).
- [59] Y. O. Nikolaieva, Y. M. Bidasyuk, K. Korshynska, E. V. Gorbar, J. Jia and A. I. Yakimenko, Phys. Rev. D **108**, 023503 (2023).
- [60] J. M. Thijssen, *Computational Physics*, (Cambridge University Press, 2007).
- [61] Y. Nesterov, Soviet Math. Dokl. **27**, 372 (1983).
- [62] W. Su, S. Boyd and E. J. Candès, J. Mach. Learn. Res. **17**, 153 (2016).
- [63] B. O'Donoghue and E. J. Candès, Found. Comput. Math. **15**, 715 (2015).
- [64] Y. Castin and R. Dum, Phys. Rev. Lett. **77**, 5315 (1996).
- [65] K. Hayashi, M. Ibe, S. Kobayashi, Y. Nakayama and S. Shirai, Phys. Rev. D **103**, 023017 (2021).
- [66] D. S. Jin, J. R. Ensher, M. R. Matthews, C. E. Wieman and E. A. Cornell, Phys. Rev. Lett. **77**, 420 (1996).
- [67] M. -O. Mewes, M. R. Andrews, N. J. van Druten, D. M. Kurn, D. S. Durfee, C. G. Townsend and W. Ketterle, Phys. Rev. Lett. **77**, 988 (1996).
- [68] C. Deppner, W. Herr, M. Cornelius, P. Stromberger, T. Sternke, C. Grzeschik, A. Grote, J. Rudolph, S. Herrmann, M. Krutzik, A. Wenzlawski, R. Corgier, E. Charon, D. Guéry-Odelin, N. Gaaloul, C. Lämmerzahl, A. Peters, P. Windpassinger and E. M. Rasel, Phys. Rev. Lett. **127**, 100401 (2021).
- [69] D. Lai, F. A. Rasio and S. L. Shapiro, ApJS, **88**, 205 (1993).